Argon adsorption in open-ended single-wall carbon nanotubes

S. Rols,[1] M. R. Johnson,[2] P. Zeppenfeld,[3,*] M. Bienfait,[4] O. E. Vilches,[5] and J. Schneble[5]

[1]*Groupe de Dynamique des Phases Condensées, Université Montpellier II, F-34095 Montpellier Cedex 05, France*
[2]*Institut Laue-Langevin, B.P. 156, F-38042 Grenoble Cedex 9, France*
[3]*Institut für Experimentalphysik, Johannes Kepler Universität Linz, A-4040 Linz, Austria*
[4]*CRMCN-CNRS, Faculté de Luminy, Case 901, F-13288 Marseille Cedex 9, France*
[5]*Department of Physics, University of Washington, Seattle, Washington 98195-1560, USA*

Thermodynamic and neutron-diffraction measurements combined with molecular dynamics simulation are used to determine the adsorption energies and the structure of argon condensed in the various adsorption sites of purified open-ended single-wall nanotube bundles. On the basis of these experiments and the simulation results, a consistent adsorption scenario has been derived. The adsorption proceeds first by the population of the walls inside the open nanotubes and the formation of one-dimensional Ar chains in the grooves at the outer surface of the bundles, followed by the filling of the remaining axial sites inside the nanotubes and the completion of a quasihexagonal monolayer on the outer surface of the bundle. The measurements also provide an estimate of the relative abundance of the various adsorption sites revealing that a major part of the adsorbed Ar is stored inside the open-ended nanotubes. Nanotube bundles generally show a certain degree of heterogeneity and some interstitial sites should be populated over a range of Ar chemical potential. However, for the sample used here, diffraction data and simulations suggest that heterogeneity is not a key feature of the bundles and there is little direct evidence of interstitial sites being populated.

I. INTRODUCTION

There has been a great deal of interest in the adsorption of gases on single-wall carbon nanotubes because of their potential applications in hydrogen storage[1,2] or isotope separation,[3,4] in chemical sensors,[5,6] and also in their possible use as a template for one-dimensional adsorption.[7] Experimentally synthesized single-wall nanotubes (SWNTs) are known to pack into bundles forming a hexagonal lattice containing about 50 individual tubes. Each nanotube is made of a graphene sheet wrapped around itself into a seamless cylinder with a diameter of 1–2 nm and a length of a few micrometers.

Depending on the methods used to process the SWNTs, the nanotubes are either capped at both ends[8–13] or open-ended.[14–18] The main advantage of the open SWNT bundles is that they provide a larger number of adsorption sites. Hence, in addition to the closed SWNT bundles which exhibit interstitial channels between three adjacent tubes (IC sites) as well as groove (G) and surface (S) sites at the curved outer surface of the bundles, the open-ended SWNT bundles provide adsorption sites (INT) *inside* the empty nanotubes. These INT sites can be differentiated in wall sites (T) at the inner wall of the tubes and in axial sites (t) at the center of the tube neighboring to occupied T sites (Fig. 1). As a result, the adsorption capacity is significantly increased and several new structures and phase transitions are observed[17–19] or expected.[20–22]

The determination of the number of available INT, IC, G, and S sites is a challenging task. It is complicated by the fact that the SWNT samples are heterogeneous.[9,10,23–26] The heterogeneities are mainly due to remaining metal catalyst particles, amorphous carbon, and packing defects originating from the spread of diameters of the synthesized nanotubes. For instance, the lattice parameter of the quasihexagonal 2D bundle lattice is about 17 Å with a spread of ±1 Å for typical close-ended nanotube bundles.[9,27] This results in interstitial channels (ICs) with different diameters and a range of adsorption energies, limiting the adsorption of gases to only the widest interstitial channels. As for the open-ended SWNT samples, only a fraction of the nanotubes may be open and accessible for adsorption, depending on the method used to process them.[16] Generally, however, the total population of INT sites is expected to be much larger than that of the IC sites.

The detection of the population of internal sites (INT) upon gas adsorption is by no means simple. Site specificity can be achieved with adsorption isotherm measurements,[16,18,28,29] infrared spectroscopy,[30] temperature programed desorption,[14,15] electron microscopy,[19] or x-ray diffraction.[31] The use of a single characterization technique often induces some ambiguities in the determination of the proportion of the different sites on a given sample.

In previous studies[23,27,32] we have shown that thermodynamic and neutron-diffraction measurements combined with molecular dynamics simulations can be used to determine the adsorption scenario of simple species on close-ended SWNT bundles, to quantify the adsorption energies as a function of coverage, and to estimate the number of accessible IC, G, and S sites. Here we extend this work to open-ended SWNT bundles. Using the same techniques, we are able to determine the adsorption scenario and the corresponding evolution of the adsorbate structure. We will show that the adsorption proceeds first by the population of the T sites at the inner walls of the open nanotubes and the formation of one-dimensional Ar chains in the grooves (G) and some of the IC sites, followed by the population of the axial
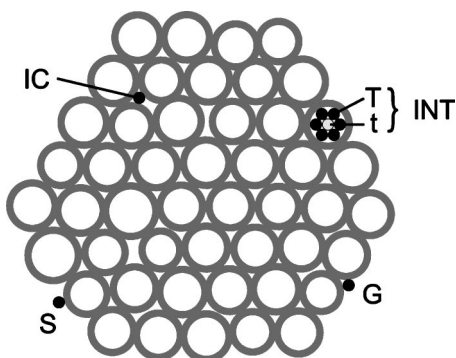
FIG. 1. Schematic section of a nanotube bundle containing $N=48$ nanotubes with an outer diameter $L=(17\pm1)$ Å. The bundle diameter is about 120 Å ($\approx\sqrt{N}L$), the total number of hollows, grooves and interstitial channels is 48 ($N_H=N$), 21 ($N_G\approx3\sqrt{N}$), and 73 ($N_{IC}\approx2N-N_G$), respectively. Depending on the number of adsorbate rows that can be accommodated at the inner walls (M_T), as central rows (M_t), and on the outer convex surface of the peripheral nanotubes, M_S, the maximum number of internal (INT=T,t) and surface (S) sites becomes $N_{INT}=(M_T+M_t)N_H$ and $N_S=M_SN_G$, respectively. Note that not all tubes have to be open-ended and that only the widest interstitial channels may be accessible to the adsorbates (black circles on G, S, IC, T sites, gray circle on an axial t site, drawn to the size of an Ar atom with 3.8 Å diameter).

sites (t) inside the nanotubes and the formation of a two-dimensional quasihexagonal monolayer at the outer surface of the bundles. We have also determined the adsorption energies as a function of coverage and assign them to the different adsorption sites. This study further illustrates the advantages and the limits of the combination of the above techniques for studying these nonuniform systems.

We use argon for our study because it adsorbs reversibly on SWNT bundles and is thus well suited for thermodynamic measurements. In addition, the ^{36}Ar isotope is known to have a large coherent neutron cross section of 77.9 barn giving rise to clear neutron-diffraction patterns that can be exploited for structural analysis.[23,27,32–34]

II. EXPERIMENT

To minimize the effect of impurities, we use a chemically purified (95%) sample of open-ended SWNT bundles provided by the MER corporation (www.mercorp.com).[17] The multistage purification process is described elsewhere.[35] Electron microscope images display virtually nothing except bundles with an average diameter of 130 Å, i.e., bundles containing about 50 nanotubes. The neutron diffraction spectra (see below) do not reveal any diffraction line from metal catalysts unlike the non purified SWNT samples,[23] and only a very small fraction of graphitized carbon. A fit of the bare SWNT diffraction peaks yields a distance between two adjacent nanotubes in a bundle of 17 ± 1 Å. The finite dispersion of the tube diameter produces a distribution in width and shape of the interstitial channels as already explained in Refs. 23–25.

A. Thermodynamics

Sets of adsorption isotherms have been recorded at four different temperatures (77, 81, 85, and 90 K) on a 27 mg
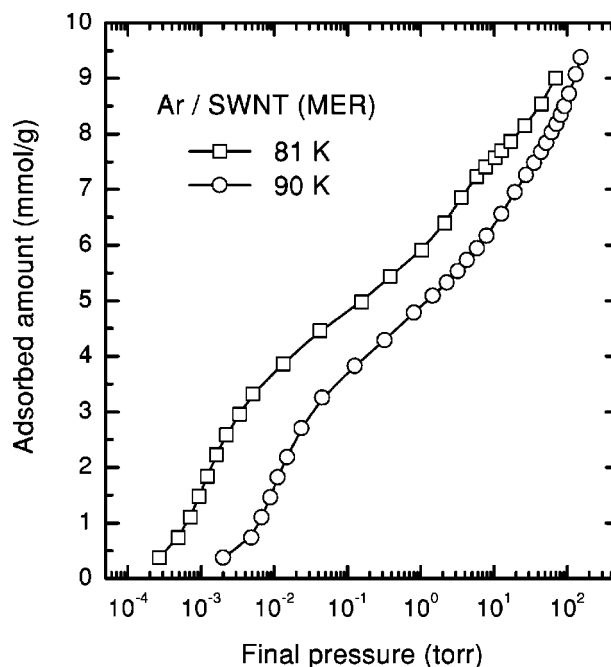

FIG. 2. Adsorbed amounts of Ar on the open-ended nanotube bundles as a function of equilibrium pressure. The adsorbed quantities were normalized to 1 g of the SWNT sample, which essentially contains carbon nanotube bundles but also amorphous and graphitized carbon. Two risers are observed between 0 and 5 mmol/g and between 5 and 7.5 mmol/g, respectively. The first riser corresponds to the filling of high energy adsorption sites (internal sites, grooves, and the widest interstitial channels, see Fig. 1). The second riser (lower binding energy) is mainly assigned to adsorption in the t sites and on the curved graphene sheets forming the outer surface of the bundles.

sample using the volumetric method.[10,11] This sample was a part of the 350 mg SWNT sample used in the neutron-diffraction experiments. The nanotubes were outgassed in the sample cell at 80 °C for several hours before the argon was introduced. The equilibration time at 77 K depends on coverage; for small Ar doses (<2 mmol/g) it takes 4 to 5 h to reach equilibrium but this time decreases to about half an hour for doses above 5 mmol/g.

The adsorption isotherms recorded at 81 and 90 K are represented in Fig. 2. The reversibility and the reproducibility of the data have been checked upon adsorption and desorption for the 81 K isotherm. From the whole set of isotherms the isosteric heat of adsorption $q_{st}=-Rd(\ln p)/d(1/T)$ is obtained from the slope of the regression line fitted to the data in a Clausius-Clapeyron plot (ln p vs $1/T$). The variation of q_{st} as a function of coverage is shown in Fig. 3.

Two risers can be seen in Fig. 2. The first one, coresponding to the high binding energy sites (first plateau in Fig. 3), is significantly larger (5 mmol/g) than the first riser obtained with nonpurified close-ended SWNT bundles (0.8 mmol/g).[10–13,32,36] The second riser at higher pressure has a height of 2.4–2.8 mmol/g, which is slightly larger than the one measured on the nonpurified close-ended SWNT bundles (1.7 mmol/g).[10–13,32,36] It is generally accepted[10,13] that these
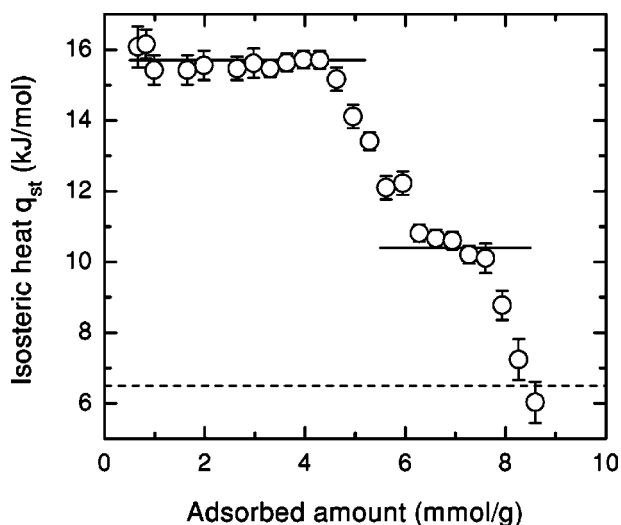
FIG. 3. Isosteric heat of adsorption q_{st} as a function of coverage (total adsorbed amount) obtained from Ar adsorption isotherms recorded at different temperatures. The two plateaus (indicated by the solid lines) correspond to the two risers in Fig. 2. For large doses q_{st} tends towards the latent heat of vaporization $q_{3D} = 6.5$ kJ/mol (dashed line).

low-energy binding sites (second plateau in Fig. 3) are located on the curved outer surfaces of the bundles (S sites). The high-energy adsorption sites are still subject to debate[10–13,25,26,32] and are thought to be a mixture of G and IC sites on close-ended nanotubes and, in addition, of INT sites if some of the nanotubes are open.[14–16,28] Note that for higher coverages, q_{st} decreases and tends towards the value of the heat of vaporization of bulk argon of 6.5 kJ/mol.

The values of the adsorption energies measured on the two plateaus in Fig. 3 (15.7 and 10.4 kJ/mol, respectively) are very close to those obtained on close-ended SWNT bundles (15 and 10 kJ/mol, respectively).[23,32,36] This is surprising because new adsorption sites (INTs) are available on the open-ended SWNT bundles which might give rise to another plateau in Fig. 3. As it turns out, however, the presence of INT sites mainly leads to an extension of the first plateau which spans a much larger coverage range on the present sample (5 mmol/g) than on the close-ended SWNT bundles (0.8 mmol/g). An explanation for this observation will be given in Sec. III.

Comparing our results to those in the literature, it seems that there is no general agreement on the binding strength of the high-energy adsorption sites. For instance, mechanically uncapped nanotubes,[16] appear to provide new sites at the interior of the open tubes with a stronger binding energy than the G sites. In a recent study, Jakubek and Simard[18] also found that the sites at the interior of the open-ended nanotubes are considerably more attractive than the groove sites, as indicated by a step in the adsorption isotherms at lower temperatures for the open tubes. Although the process used for uncapping is not the same as in our case, it is not clear, at this time, what the origin for the different binding energies inside the nanotubes could be.

A straightforward calculation[10,16] can provide an estimate of the total number of G and IC sites for our average 50 tube

bundles (see Fig. 1). This gives a maximum adsorption capacity of 0.6 and 2.1 mmol/g for the G and IC sites, respectively. Hence, we have to consider other high binding energy sites to account for the 5 mmol/g adsorbed across the first riser in Fig. 2. These sites can only be located *inside* the open nanotubes, i.e., on INT sites. Simple geometric arguments show that 6 to 7 parallel Ar rows can be accommodated inside a single nanotube. Accordingly, the maximum capacity on INT sites lies between 8 and 9.3 mmol/g. A similar argument can be used to estimate the number of S sites available on the convex outer surface of the bundles. Knowing that 4 to 5 Ar atoms can be accommodated on S sites between adjacent grooves, we find that the number of available S sites ranges between 2.4 and 3 mmol/g. If we assume that the first riser in Fig. 2 corresponds to the adsorption on the INT, G, and IC sites, we have to accept that we either overestimate the total number of these sites or, more likely, that some of the tubes are not open and that only a fraction of the INT (and of the IC) sites are accessible and occupied by argon atoms.[24–26] Still, the total amount of adsorbed argon before bulk condensation (~ 8.5 mmol/g) on our sample is much larger than on nonpurified close-ended SWNT bundles (3.5 mmol/g) (Refs. 32 and 36) and even larger than on samples where some of the nanotubes are open-ended (~ 6 mmol/g in Refs. 28, 29, and 31).

B. Neutron diffraction

A 350 mg SWNT sample, outgassed at 150 °C for one day prior to the experiment, was used for the neutron measurements. For calibration, an Ar adsorption isotherm was recorded at 77 K, before the neutron-diffraction data were taken at the D20 neutron diffractometer at the ILL. The diffraction patterns were recorded using a wavelength $\lambda = 2.414$ Å and a scattering vector range 0.2 Å$^{-1} < Q < 5$ Å^{-1}.

Several argon doses (coverages) were investigated (0.64, 1.27, 2.55, 3.83, 5.10, and 8.93 mmol/g) in order to explore the different adsorption sites and argon structures. All experiments, including the diffraction from the bare sample (background), were performed at 10 K, except one for 1.27 mmol/g, which was also recorded at 40 K. We did not observe any significant changes for this argon dose when raising the temperature from 10 to 40 K.

The argon gas was slowly introduced or incremented— typically over a period of one to two hours—into the aluminum sample cell at temperatures for which the pressure could be controlled during the major part of the adsorption (100 K for the lowest dose to 70 K for the largest). Once the measuring temperature (10 or 40 K) was reached after about one hour, neutron-diffraction spectra were accumulated in steps of half an hour. Each time, we checked that no evolution of the diffraction pattern took place between successive spectra, indicating that equilibrium had been reached. The total measuring time was of the order of 6 to 10 hours for each coverage.

The diffraction pattern for the bare SWNT sample is shown in Fig. 4. The narrow lines at 2.74 Å^{-1}(Al), 3.14 Å^{-1}(Al), 4.49 Å^{-1}(Al$_2$O$_3$) are due to the aluminum cell,
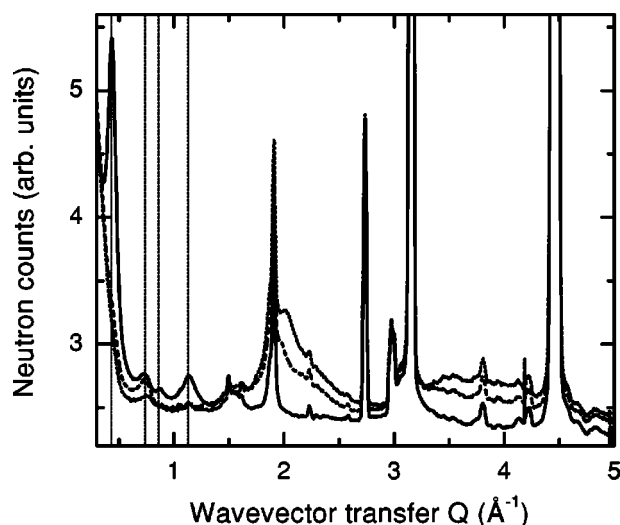
FIG. 4. Neutron-diffraction spectra of the bare SWNT bundles (solid line) and upon adsorption of 5.1 mmol/g (dashed line, top of the first riser in Fig. 2) and 8.93 mmol/g (dotted line, top of the second riser in Fig. 2) of ^{36}Ar. The vertical lines indicate the positions of the Bragg diffraction peaks expected for a hexagonally close packing of the nanotubes with a bundle lattice spacing of 17 Å. The narrow peaks arise from the aluminum cell, from the carbon skeleton of the nanotube, and from graphitic carbon impurities.

the one at 2.97 Å^{-1} corresponds to the (100) diffraction peak of the graphene planes, and those at 1.9 and 3.8 Å^{-1} result from the (002) and (004) peaks of graphitized carbon. The lines at 0.43, 0.74, 0.85, and 1.13 Å^{-1} correspond to the hexagonal packing of the SWNTs into bundles; they are labeled (10), (11), (20), and (21), respectively. Fitting these peaks to a series of Gaussians superimposed on a smooth background reveals that the relative intensities and the peak widths (and, hence, the average bundle size and tube diameter distribution) for the present MER sample are similar to those of the close-ended SWNT bundles used in our previous studies. On the other hand, the much lower background indicates a significantly smaller concentration of highly irregular bundles and other impurities in the MER sample.

After ^{36}Ar adsorption the diffraction pattern of the SWNT bundles changes significantly from the one measured without adsorbate. As an illustration we have plotted in Fig. 4 the diffraction spectra obtained for 5.10 mmol/g (top of the first riser in Fig. 2) and for 8.93 mmol/g (top of the second riser in Fig. 2) of adsorbed argon. We observe a drop of the intensity between 0.35 and 1.3 Å^{-1} and broad contributions located between 1.5 and 2.8 Å^{-1} and between 3.2 and 4.7 Å^{-1}. These adsorption induced changes are more clearly visible in Fig. 5 where the difference spectra (^{36}Ar on bundles minus bare bundles) for all measured doses are shown. No corrections for neutron absorption by ^{36}Ar were made. In fact, there is no visible attenuation of the Al, Al$_2$O$_3$, and graphitized carbon peaks upon Ar adsorption in Fig. 4.

The negative intensity observed below $Q = 1.5$ Å^{-1} arises from the cross interference between the adsorbate and the SWNT skeleton of the bundles.[24,31,32] For the same reason, the intensity of the (10) line (assigned to the first order Bragg peak of the hexagonal bundle lattice) drops steadily upon Ar
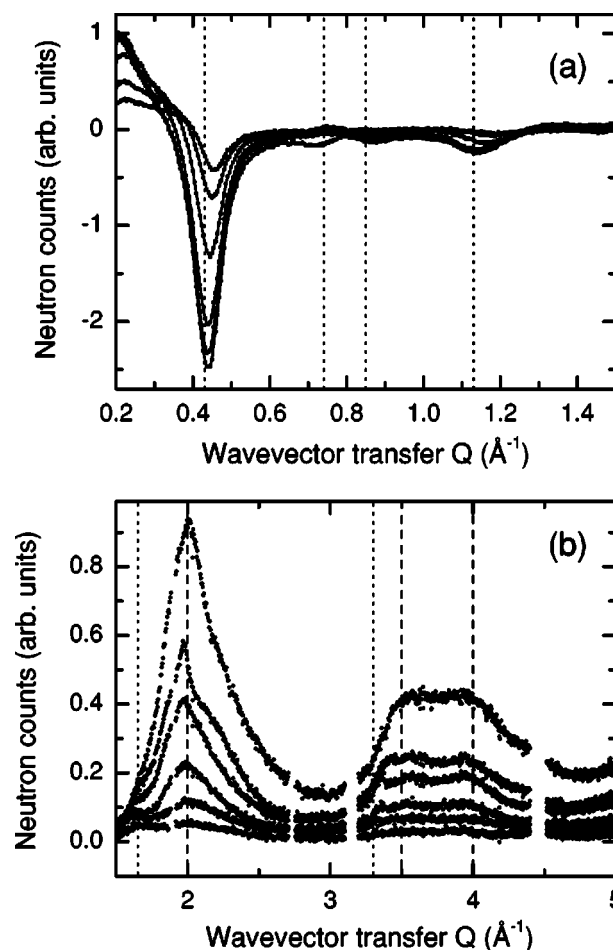

FIG. 5. Diffraction difference spectra (after subtraction of the bare SWNT spectrum) for several Ar doses (0.64, 1.27, 2.55, 3.83, 5.10, and 8.93 mmol/g). (a) Small wave vector region ($Q \leqslant 1.5$ Å^{-1}). The intensity of the main (10) Bragg peak at 0.43 Å^{-1} decreases monotonously with Ar coverage (curves from top to bottom). The dashed lines indicate the positions of the Bragg diffraction peaks expected for a hexagonally close packing of the nanotubes with a bundle lattice spacing of 17 Å. (b) Large wave vector region ($Q \geqslant 1.5$ Å^{-1}), showing the evolution of ordered Ar structures (increasing intensities with increasing Ar coverage, curves from bottom to top). The vertical lines indicate the peak positions expected for Ar condensed in linear chains (dotted lines) and in 2D hexagonal arrays (dashed lines). Sharp double-spiked features in the difference spectra, arising from the contributions of the cell and amorphous carbon, have been removed from the spectra.

adsorption, whereas the variation of the (11), (20), and (21) Bragg peaks is not monotonous [Fig. 5(a)].

The broad components centered around 2 and between 3.5 to 4 Å^{-1} [Fig. 5(b)] are composed of Ar Bragg peaks related to the medium range order of the Ar atoms arranged in chains or small hexagonal patches. A more detailed analysis reveals that the intensity contribution located at about 1.65 and the onset at 3.3 Å^{-1} [dotted vertical lines in Fig. 5(b)] are due to the first and second order diffraction lines, respectively, of linear chains of Ar atoms with interatomic spacing of 3.8 Å and that the 2, 3.5, and 4 Å^{-1} peaks [dashed vertical lines in Fig. 5(b)] are first and higher order diffraction lines

of pseudo-hexagonal patches in which rows of Ar atoms are spaced at $\sqrt{3}a/2 \approx 3.2$ Å where a is again the (slightly compressed) distance between neighboring Ar atoms of about 3.7 Å.

The 1.65 and 2 Å^{-1} peaks coexist from the very beginning of the Ar adsorption (0.64 mmol/g). From 0.64 to 1.27 mmol/g both contributions increase. For higher coverages, the 1.65 Å^{-1} peak remains essentially constant while the 2 Å^{-1} contribution continuously increases.

III. COMPUTER SIMULATION

A. Model description

All calculations were performed using the CERIUS^2 and the MATERIAL STUDIO molecular modeling software packages. The SORPTION tool of CERIUS^2 allowed a Monte Carlo search of the different adsorption sites on a rigid substrate to be performed as a function of adsorbate pressure and temperature. The DISCOVER module of MATERIAL STUDIO was used to perform energy minimizations of the different set of structures to give stable configurations, including all atomic degrees of freedom. In this work, only the COMPASS force field was used, which has been developed from a wealth of experimental and *ab initio* data.[37] This force field shows the correct physical trends and we have not varied parameters simply to reproduce our experimental results. Finally, the amorphous diffraction module of CERIUS^2 was used to calculate the diffraction patterns of finite size models by applying the Debye formula. Further details of the calculation methods are reported in a previous article.[24]

In this work, three different models were considered and will be denoted as Mhetero, Mhomo1, and Mhomo2 in the following. The Mhetero model was developed in the context of earlier work on methane adsorption in bundles of closed nanotubes[24] in which 19 tubes of different diameters were included in the bundle in order to investigate methane adsorption in IC sites. That work was focused on the effect of populated IC sites on the principal bundle diffraction peak but the calculated overall diffraction patterns were also in good agreement with the experimental data obtained from the "Montpellier" nanotubes. The MER sample gives higher quality diffraction data mainly due to the higher purity of the sample which leads to a weaker background in the diffraction patterns. When confronted with this data, the Mhetero model appears to be too heterogeneous to accurately represent the MER sample. While, in principle, a range of Mhetero models with different packing of tubes with a Gaussian diameter distribution could have been studied, computational cost leads us to consider more regular models based on the most common (10, 10) tubes, containing 19 and 37 tubes for models Mhomo1 and Mhomo2, respectively. Both of these models give better agreement with the diffraction data than the Mhetero model. The hexagonal lattice parameter is 16.8 Å. Bundle size effects were evident with the smaller of these models when considering the higher order bundle reflections in the Q range below 1.5 Å^{-1}. Thus the 37-tube model has been retained as being the most realistic and all diffraction results presented below were obtained for this model.

A key feature of the Mhetero model was the flexibility of the tubes that allows tubes of different diameters to pack compactly in a bundle and to "envelope" adsorbed atoms and molecules in different size IC sites, modifying the stability of these particular sites. The binding energies for Ar in IC sites in the Mhetero model have been calculated in this work (see below). The Mhomo models could have been constructed from rigid tubes since the packing of identical tubes and the binding energies in INT, G, and S sites does not depend on the tube flexibility. However, all atomic degrees of freedom have been retained in this work which, therefore, only has an impact on the calculation of the binding energy in the IC sites in the Mhomo models. Adsorption calculations and energy optimization were performed on periodic models of length 19.6 Å. For closed tubes as in Ref. 24 the internal volume of the nanotubes had to be specifically excluded in the adsorption simulations, whereas for the simulations on open tubes presented here, any free volume in the model is populated. This difference in method arises from the use of periodic models (i.e., infinitely long tubes) in which there is no physical distinction between open-ended and closed tubes. Diffraction calculations used finite size models made of four periodic units, i.e., nanotubes with a total length of $4 \times 19.6 = 78.4$ Å.

B. Adsorption and binding energies

Adsorption simulations were performed on the three models at 10 kPa and 80 K in order to have the totality of the INT, G, and S adsorption sites occupied. Following energy optimization, which corresponds to cooling the sample to 0 K, reasonably well-ordered adsorbate structures were obtained. Linear chains of Ar atoms, with typical interatomic spacing of ~3.8 Å, are found in G sites (one chain per G site) and in INT sites [six chains close to the tube wall (T) and a seventh along the tube axis (t)]. The chains in the INT sites are translated with respect to another, giving a curved hexagonal structure around the inner wall of the tube. Otherwise hexagonal packing (lattice parameter 3.8 Å) is observed on the S sites which is commensurate with the G-G separation. Each hexagon has a side parallel to the grooves.

Binding energies of Ar on nanotube substrates are dominated by the Ar-C interaction. They are therefore calculated for G, S, T, or IC sites by optimizing the position of a single Ar atom in the corresponding site and evaluating the energy difference

$$E_i = \frac{1}{n(i)}(E_{\text{tube}} - E_{\text{tube}+n(i)}),\tag{1}$$

where $n(i)$ is the number of Ar atoms adsorbed at site i with i=G, S, T, or IC. For the t site the binding energy is calculated from the fully loaded tube as

$$E_{\text{t}} = \frac{1}{n(\text{t})}(E_{\text{tube}+n(\text{T})} - E_{\text{tube}+n(\text{T})+n(\text{t})}).\tag{2}$$

The binding energies are $E_G = 19.7$ kJ/mol, $E_S = 13.4$ kJ/mol, $E_T = 21.3$ kJ/mol, and $E_{\text{t}} = 14.7$ kJ/mol. These values are about 30% too big but show the correct relative stability of the sites.

The axial sites t have previously been considered by Gatica *et al.*[21,22] in a theoretical study of the properties of strongly anisotropic quantum fluids but, to the best of our knowledge, no adsorption energy for Ar adsorbed in these sites have been published so far. Stan *et al.*[38] report values of 11.8 and 13.4 kJ/mol for the T and G sites, respectively, while Maddox and Gubbins[39] find that the adsorption energies range between 16 to 19 kJ/mol depending on the Ar coverage.

IC sites are not populated in the adsorption part of the simulation since these sites are the least stable on a *rigid* substrate. However, during energy optimization with all atomic degrees of freedom these sites become much more stable. The IC sites were thus populated by hand. The binding energy is calculated using Eq. (1) for a *filled* IC channel to take into account strong, effective Ar-Ar interactions due to the distortion of the nanotubes (see Ref. 24). E_{IC} is found to be 8.0 kJ/mol for a homogenous bundle of (10, 10) nanotubes. In the heterogenous bundle E_{IC} ranges from 4.2 to 18.8 kJ/mol, depending on the packing of different diameter tubes. E_{IC} is the only binding energy that depends on C-C interactions since it is determined by bundle packing-induced and Ar-induced deformations of the nanotubes. The COMPASS force field used here gives softer tubes, tighter bundle packing and smaller binding energies than the DREIDING force field that was used previously for equivalent calculations with methane.[24]

The above binding energies can be grouped and ranked as $E_T \sim E_G > E_t \sim E_S$. The two risers in the adsorption isotherm are, therefore, attributed to the population of T and G sites at low pressure and t and S sites at higher pressure, as mentioned in the experimental section. IC sites may be populated throughout the pressure range accounting for a sloping background in the isotherm.

C. Diffraction diagram

The diffraction diagram of the optimized, Mhomo2-based models for various Ar coverages was calculated using the amorphous diffraction module of CERIUS[2]. Difference diffraction patterns were obtained by subtracting the pattern of the bare nanotubes from that of the bundles with different sites populated according to the above scenario. Figure 6 shows an overview of the simulation results that can be compared with Fig. 5. The three simulated patterns correspond to the T sites of 10 out of the 37 tubes being filled, all T and G sites occupied, and, finally, T, t, G, and S sites populated. The equivalent experimental loadings would be 2.55, 5.10, and 8.93 mmol/g.

Overall, the agreement between simulation (Fig. 6) and experiment (Fig. 5) is very good, with both features and trends in the measured diffraction patterns being reproduced by the simulations. The principal, (1,0) bundle peak at $\sim$0.45 Å^{-1} decays in intensity with loading of the INT sites and a deep minimum appears in the difference patterns. At $\sim$1.6 Å^{-1} a small peak is observed at low Ar coverages due to linear chains of Ar in T sites with interatomic spacing of $\sim$3.9 Å. Populating the T sites also gives a maximum at $\sim$2 Å^{-1} due to the pseudohexagonal packing of Ar on the
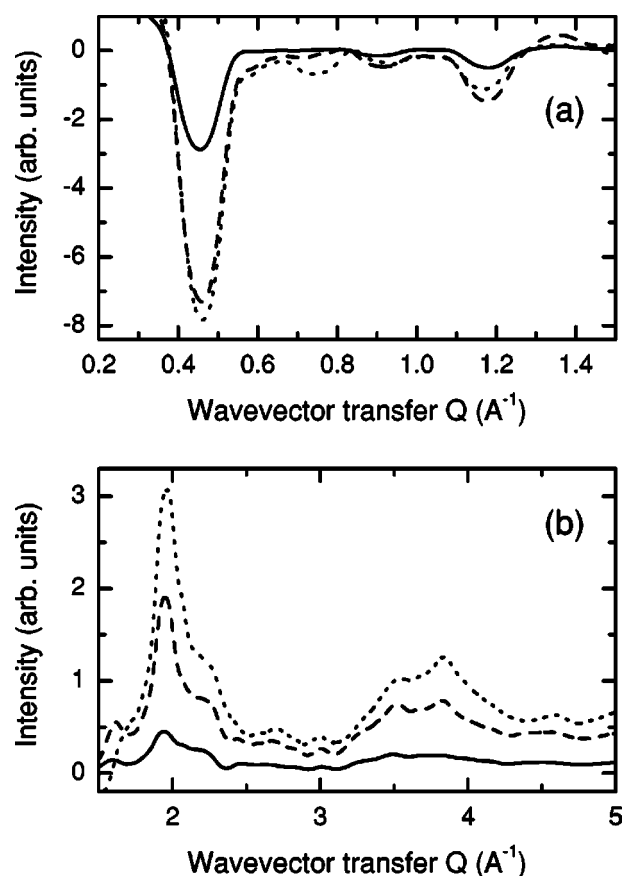

FIG. 6. Calculated diffraction spectra (after subtraction of the bare SWNT contribution) for several Ar doses adsorbed on a homogeneous 37 nanotube bundle (Mhomo2 model). (a) Small wave vector region ($Q \le 1.5$ Å^{-1}), (b) large wave vector region ($Q \ge 1.5$ Å^{-1}). Solid line: after filling the T sites of 10 out of the 37 tubes; dashed line: all T and G sites are populated; dotted line: in addition, all the S sites and t sites are occupied. A good overall agreement between simulation and experiment (Fig. 5) is obtained.

inner walls of the tubes, with a lattice parameter of $\sim$3.7 Å. The $(1,1)_{Ar}$ reflection of this hexagonal structure appears close to 3.5 Å^{-1} and the $(2,0)_{Ar}$ reflection at 4 Å^{-1}. The hexagonal structure that forms on the S sites at higher coverages reinforces the high Q intensity, although the curvature of the pseudo-2D structures on the inner and outer tube walls are not the same and an average pattern is observed. The ratio of the minimum to the maximum intensity is close to 8/3, as in the data.

The intensity of the principal bundle peak at $\sim$0.45 Å^{-1} decays monotonically with loading, giving a continuously deepening minimum in the difference patterns, even when the S sites are populated. The progressive loading of T sites at low pressure is confirmed by the strong dependence of the depth of the minimum on the number of such sites that are occupied. When all T sites are occupied, the minimum is almost at its deepest. Populating the S sites would normally reduce the depth of the minimum,[24] but since the t sites are populated at about the same pressure, the net effect is a further deepening of the minimum.

A closer look at the higher order bundle peaks up to 1.5 Å^{-1} is shown in Fig. 7. The simulation results [Fig. 6(a)],
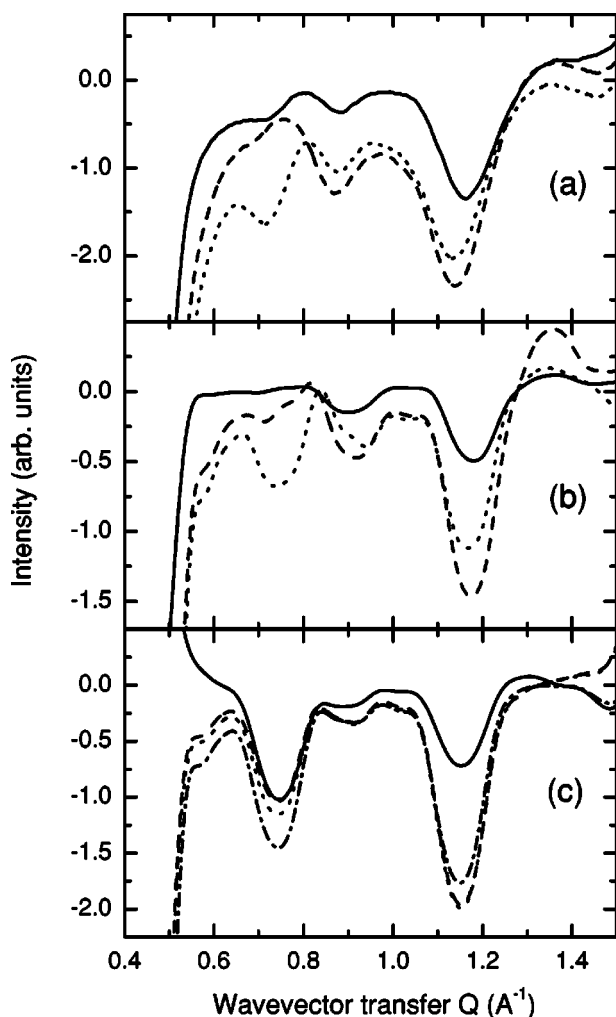
FIG. 7. Details of the evolution of the difference spectra in the region of the higher order bundle lattice peaks. (a) Experimental data, replotted from Fig. 5(a) with the solid, dashed, and dotted lines corresponding to Ar doses of 2.55, 5.10, and 8.93 mmol/g, respectively. (b) Calculated diffraction difference spectra as in Fig. 6(a) with the solid, dashed, and dotted lines corresponding to the filling of the T sites of 10 out of the 37 tubes, all T and G sites, and all T, G, S, and t sites, respectively. (c) Calculated diffraction difference spectra showing the influence of the adsorption on the IC sites on the diffraction pattern. Solid line: all IC sites filled; dashed line: all IC and T sites filled; dotted line: all IC, T, and G sites filled; dash-dotted line: all IC, T, G, and S sites filled.

lated curve [solid lines in Figs. 7(a) and 7(b)].

Figure 7(c) shows a corresponding set of diffraction patterns when all IC sites are occupied. These patterns show negligible peak and minima shifts on loading, unlike the data in Fig. 7(a) and the models with no IC sites occupied [Fig. 7(b)], suggesting that the population of IC sites is not so significant in the rather homogeneous MER sample. Yet, comparing the dashed lines in Figs. 7(b) and 7(c) corresponding to the filling of the T and G sites without and with IC sites filled, respectively, one notices that the bump appearing in Fig. 7(b) at around 1.35 $Å^{-1}$ is suppressed in Fig. 7(c). Since this bump is not seen in the experimental spectrum [dashed line in Fig. 7(a)] we may infer that some of the IC sites are populated. Another possible indication for IC population is found at higher Q. In the data [Fig. 5(b)], there is a clear horizontal plateau between 3.5 and 4.0 $Å^{-1}$, whereas in the calculations [Fig. 6(b)] the spectrum reveals two peaks within the same Q range. Calculations with all IC sites loaded show a weakening of the intensity around 4.0 $Å^{-1}$ with increasing Ar coverage (not represented here), so populating a few IC sites would better reproduce the measured difference diffraction pattern in this Q range.

IV. CONCLUSION

We have studied the adsorption of argon in purified bundles of open-ended single-wall carbon nanotubes. These bundles exhibit a very large adsorption capacity and provide a great variety of adsorption sites located inside the tubes (INT), in the interstitial channels between tubes (IC), in the grooves (G), and on the curved part of the outer surface of the bundles (S), respectively. In view of these different adsorption sites, the result of the thermodynamics measurements is rather surprising, as only two sets of adsorption energies at about 15.7 and 10.4 kJ/mol are obtained (see Fig. 3). This puzzling observation is explained with the help of atomistic total energy calculations. It is shown that inside the tubes two types of INT sites can be distinguished: T sites located on the inner walls of the nanotubes and axial sites (t) which become populated when the T sites are filled. For Ar atoms the T sites have about the same high adsorption energy than the G sites and the widest interstitial channels (IC). The low-energy adsorption sites comprise the S, the t, and some of the IC sites. The large amount of argon adsorbed at small chemical potential is a clear indication for the large number of Ar that can be stored *inside* the open-ended MER nanotubes. This interpretation is confirmed by neutron diffraction experiments which reveal a continuous drop of the intensity of the (10) bundle lattice peak as a function of Ar coverage. The position of the bundle diffraction lines does not change very much, indicating that the adsorption does not modify significantly the overall bundle packing. In addition, the argon related diffraction features at higher wave vectors $Q > 1.5$ $Å^{-1}$ reveal that the argon adsorbed at the T sites, the linear chains on the G, IC, and t sites, as well as the pseudohexagonal patches on the S sites are poorly organized with only a limited medium-range order. Finally, the combination of thermodynamics and neutron-diffraction experiments enable us to estimate the amount adsorbed in the dif-

depicted again in Fig. 7(b), reveal trends and details in good agreement with the experimental data shown in Fig. 7(a). In the region of the (1,1) bundle reflection at ~0.75 $Å^{-1}$, the minimum is most pronounced at highest loading and the position of the maximum at ~0.85 $Å^{-1}$ is upshifted as the loading is increased. The minimum in the region of the (2,1) bundle reflection at ~1.15 $Å^{-1}$ is deepened and downshifted upon loading. Also, the calculated crossover in intensity between the two highest coverages, such that the minima at ~0.9 and ~1.2 $Å^{-1}$ are deepest when only the T and G sites are populated, matches the trends in the data [Fig. 7(a)]. However, the data reveal a clear maximum at ~0.8 $Å^{-1}$ at low coverage which is not correctly reproduced by the simu-

ferent sites and to propose the following adsorption scenario: The T sites on the inner walls of the nanotubes and the groove G sites on the outer bundle surface are populated first, followed by the filling of the axial t sites inside the tubes and the S sites on the outer bundle surface. A few interstitial sites are progressively populated as a function of the Ar chemical potential. Direct evidence for the population of IC sites is limited since thermodynamic and diffraction signals are dominated by the population of INT sites.

*Electronic address: peter.zeppenfeld@jku.at

[1] M. S. Dresselhaus, K. A. Williams, and P. C. Eklund, MRS Bull. **24**, 45 (1999).

[2] A. C. Dillon and M. J. Heben, Appl. Phys. A: Mater. Sci. Process. **72**, 133 (2001).

[3] Q. Wang, S. R. Challa, D. S. Sholl, and J. K. Johnson, Phys. Rev. Lett. **82**, 956 (1999).

[4] S. R. Challa, D. S. Sholl, and J. K. Johnson, Phys. Rev. B **63**, 245419 (2001).

[5] P. G. Collins, K. Bradley, M. Ishigami, and A. Zettl, Science **287**, 1801 (2000).

[6] S. H. Jhi, S. G. Louie, and M. L. Cohen, Phys. Rev. Lett. **85**, 1710 (2000).

[7] M. M. Calbi, M. W. Cole, S. M. Gatica, M. J. Bojan, and G. Stan, Rev. Mod. Phys. **73**, 857 (2001).

[8] C. Journet, W. K. Maser, P. Bernier, A. Loiseau, M. Lamy de la Chapelle, S. Lefrant, P. Deniard, R. Lee, and J. E. Fisher, Nature (London) **388**, 756 (1997).

[9] S. Rols, R. Almairac, L. Henrard, E. Anglaret, and J. L. Sauvajol, Eur. Phys. J. B **10**, 263 (1999).

[10] M. Muris, N. Dufau, M. Bienfait, N. Dupont-Pavlovsky, Y. Grillet, and J-P. Palmari, Langmuir **16**, 7019 (2000).

[11] M. Muris, N. Dupont-Pavlovsky, M. Bienfait, and P. Zeppenfeld, Surf. Sci. **492**, 67 (2001).

[12] S. Talapatra and A. D Migone, Phys. Rev. Lett. **87**, 206106 (2001).

[13] S. Talapatra and A. D. Migone, Phys. Rev. B **65**, 045416 (2002).

[14] A. Kuznetsova, D. B. Mawhinney, V. Naumenko, J. T. Yates, J. Liu, and R. E. Smalley, Chem. Phys. Lett. **321**, 292 (2000).

[15] A. Kuznetsova, J. T. Yates Jr., J. Liu, and R. E. Smalley, J. Chem. Phys. **112**, 9590 (2000).

[16] M. R. Babaa, I. Stepanek, K. Masenelli-Varlot, N. Dupont-Pavlovsky, E. McRae, and P. Bernier, Surf. Sci. **531**, 86 (2003).

[17] A. I. Kolesnikov, J.-M. Zanotti, C.-K. Loong, P. Thiyagarajan, A. P. Moravsky, R. O. Loutfy, and C. J. Burnham, Phys. Rev. Lett. **93**, 035503 (2004).

[18] Z. J. Jakubek and B. Simard, Langmuir **20**, 5940 (2004).

[19] X. Fan, E. C. Dickey, P. C. Eklund, K. A. Williams, L. Grigorian, R. Buczko, S. T. Pantelides, and S. J. Pennycook, Phys. Rev. Lett. **84**, 4621 (2000).

[20] V. V. Simonyan, J. K. Johnson, A. Kuznetsova, and J. T. Yates, Jr., J. Chem. Phys. **114**, 4180 (2001).

[21] S. M. Gatica, G. Stan, M. M. Calbi, J. K. Johnson, and M. W. Cole, J. Low Temp. Phys. **120**, 337 (2000).

[22] S. M. Gatica, M. W. Cole, G. Stan, J. M. Hartman, and V. H. Crespi, Phys. Rev. B **62**, 9989 (2000).

[23] M. Bienfait, P. Zeppenfeld, N. Dupont-Pavlovsky, J.-P. Palmari, M. R. Johnson, T. Wilson, M. De Pies, and O. E. Vilches, Phys. Rev. Lett. **91**, 035503 (2003).

[24] M. R. Johnson, S. Rols, P. Wass, M. Muris, M. Bienfait, P. Zeppenfeld, and N. Dupont-Pavlovsky, Chem. Phys. **293**, 217 (2003).

[25] W. Shi and J. K. Johnson, Phys. Rev. Lett. **91**, 015504 (2003).

[26] W. Shi and J. K. Johnson, Phys. Rev. B (to be published).

[27] M. Bienfait, P. Zeppenfeld, N. Dupont-Pavlovsky, M. Muris, M. R. Johnson, T. Wilson, M. DePies, and O. E. Vilches, Physica B **350**, 423 (2004).

[28] D. H. Yoo, G. H. Rue, J. Y. Seo, Y. H. Hwang, M. H. W. Chan, and H. K. Kim, J. Phys. Chem. B **106**, 9000 (2002).

[29] M. Eswaramoorthy, R. Sen, and C. N. R. Rao, Chem. Phys. Lett. **304**, 207 (1999).

[30] O. Byl, P. Kondratyuk, S. T. Forth, S. A. Fitzgerald, L. Chen, J. K. Johnson, and J. T. Yates, Jr., J. Am. Chem. Soc. **125**, 5889 (2003).

[31] A. Fujiwara, K. Ishii, H. Suematsu, H. Kataura, Y. Maniwa, S. Suzuki, and Y. Achiba, Chem. Phys. Lett. **336**, 205 (2001).

[32] M. Bienfait, P. Zeppenfeld, N. Dupont-Pavlovsky, M. Muris, M. R. Johnson, T. Wilson, M. DePies, and O. E. Vilches, Phys. Rev. B **70**, 035410 (2004).

[33] H. Taub, K. Carneiro, J. K. Kjems, L. Passell, and J. P. McTague, Phys. Rev. B **16**, 4551 (1977).

[34] C. Tiby and H. J. Lauter, Surf. Sci. **117**, 277 (1982).

[35] I. W. Chiang, B. E. Brinson, A. Y. Huang, P. A. Willis, M. J. Bronikowski, J. L. Margrave, R. E. Smalley, and R. H. Hauge, J. Phys. Chem. B **105**, 8297 (2001).

[36] T. Wilson, A. Tyburski, M. R. De Pies, O. E. Vilches, D. Becquet, and M. Bienfait, J. Low Temp. Phys. **126**, 403 (2002).

[37] H. Sun, J. Phys. Chem. **102**, 7738 (1998).

[38] G. Stan, M. J. Bojan, S. Curtarolo, S. M. Gatica, and M. W. Cole, Phys. Rev. B **62**, 2173 (2000).

[39] M. W. Maddox and K. E. Gubbins, Langmuir **11**, 3988 (1995).